JAAS



PAPER

View Article Online
View Journal | View Issue



Cite this: *J. Anal. At. Spectrom.*, 2021, **36**, 1055

Radially resolved optical emission spectral imaging study of an atmospheric pressure μDBD jet for elucidating the effect of sample surface material on the underlying mechanisms †

Songyue Shi, Kevin Finch and Gerardo Gamez **D**

Dielectric barrier discharges are receiving increasing attention as sampling/ionization sources for ambient mass spectrometry. Nevertheless, the underlying mechanisms are not completely understood, particularly when the plasma plume is exposed to a sample surface. Herein, an atmospheric pressure helium microdielectric barrier discharge (µDBD), flowing into open-air and onto a sample surface (floating Cu or LDPE), is studied via optical emission spectroscopy (OES) with radial information extracted through Abel's inversion. Radially resolved optical emission profiles along the axis are shown to shift with respect to the line-of-sight counterparts, for some species. The OES images, as well as vibrational and rotational temperature maps, indicate the energy transfers mainly via Penning ionization of N2 with He metastables to produce N_2^+ , as the plasma plume exits the capillary into open air, while charge transfer with He_2^+ is dominant further downstream, as well as toward the periphery of the plume. In addition, the sample surface is shown to play an important role in the energy transfer mechanisms. For the LDPE sample, the spatial distribution sequence of excited species is similar to the free-flowing counterpart but disappears into the surface, which indicates that excited N₂ further downstream/outer periphery is produced from electron recombination with N2+. On the other hand, the presence of the floating Cu sample results in an intensity peak at the plasma/surface interface for most species. We propose that the temporal evolution of the half-cycle dynamics have a great effect, where the resulting higher electron temperature and density towards the surface of metallic samples favors electron impact excitation. Furthermore, profilometry of the resulting craters in the floating Cu samples revealed a close correlation between their diameter and the width of the N_2^+ emission.

Received 21st December 2020 Accepted 6th April 2021

DOI: 10.1039/d0ja00522c

rsc.li/jaas

Introduction

Direct solid surface sampling capabilities represent a significant advantage when it comes to chemical analysis.¹ For example, all the time and resource consuming sample preparation steps involved in transforming a fraction of a sample into a suitable state for analysis by a technique of interest are avoided, while possibly allowing *in situ* sample analysis to be completed in the field. Furthermore, it may provide access to additional dimensions not typically accessible after sample preparation, such as in the case of depth profiling.

Atmospheric pressure plasma jets (APPJs) have been gaining increased interest for direct solid surface analysis.²⁻⁴ For example, plasma-based ambient mass spectrometry sources allow desorption and ionization from solid sample surfaces to give

Texas Tech University, Department of Chemistry and Biochemistry, Lubbock, TX 79409-41061, USA. E-mail: Gerardo.gamez@ttu.edu

 \dagger Electronic supplementary information (ESI) available. See DOI: $10.1039/d0 \\ ja00522c$

access to molecular and structural information from the analyte of interest in real-time. 5,6 These sources are typically configured to minimize damage to the sample surface of interest. Recently, an atmospheric pressure dielectric barrier discharge was proposed for the direct solid sampling of metal substrates, where the operating conditions allowed the substrate to be eroded and the removed material was transported to an inductively coupled plasma for mass spectrometry (MS) analysis. Additionally, depth profiling capabilities were demonstrated in that study. Our laboratory is also currently exploring the possibility of implementing a micro dielectric barrier discharge (μ DBD) for direct MS analysis of solid polymer surfaces where the operating conditions are chosen to allow erosion of the substrate for potential depth profiling capabilities.

On the other hand, the underlying mechanisms of such plasma sources are not completely understood. These fundamental processes include the production of relevant plasma reagents and the mechanisms that lead to the analytical signal. In fact, very few plasma diagnostic studies on APPJs relevant for chemical analysis have examined the influence of the sample **JAAS Paper**

surface on such fundamental processes, but these works have reported significant changes on some relevant plasma species, such as He metastables.8 Thus, plasma diagnostic studies are needed to gain more information into these mechanisms. There are many techniques, with accompanying advantages and disadvantages, that can yield critical information regarding the fundamental processes. Optical emission spectroscopy (OES) imaging allows obtaining the distribution of excited species in the plasma, which can yield valuable insights into the energy distribution pathways.9-11 In addition, relevant species give access to calculating fundamental parameters such as the vibrational temperature (T_{vib}) , 12,13 rotational temperature $(T_{\rm rot})$, ¹⁴ and excitation temperature $(T_{\rm exc})^{15}$ through Boltzmann plots, while electron number density (n_e) and electron temperature (T_e) can be obtained via Stark broadening. 16 OES diagnostics techniques are popular because they are simple, costeffective, and do not perturb the plasma. On the other hand, OES diagnostics have some disadvantages including the emission signal being inherently integrated along the line-of-sight (LOS), which does not allow to directly measure the emission intensity three-dimensional distribution, thermodynamic equilibrium (LTE) has to be assumed for obtaining some of the fundamental parameters.

The main goal of the present study is to obtain further understanding of the underlying mechanisms of APPIs relevant for chemical analysis when the plasma effluent is exposed to different sample surfaces. For this purpose, radially resolved OES plasma diagnostics of an atmospheric pressure µDBD are realized with a sub-pixel shifting push-broom hyperspectral imaging system (SPS-PbHSI).17 The radially resolved information is extracted with a previously developed protocol for Abel's inversion reconstruction based on a Discreet Fourier Transform (DFT) algorithm. 18 The distribution of excited He I, He₂, N₂, N₂, O I, as well as T_{rot} and T_{vib} maps, as a function of the μDBD operating conditions are measured in the presence of different sample surfaces. In addition, the maps are correlated to the μDBD electrical characteristics and the properties of the produced craters. Finally, some insights into the underlying mechanisms are discussed in context with relevant literature.

Experimental

Pushbroom hyperspectral imaging

The plasma OES images were acquired with a push-broom hyperspectral imaging system (Pb-HSI), 19,20 which allows the collection of hyperspectral datacubes within short acquisition time and high light throughput (Fig. S1†). In this system, the emission from the plasma source was collected by a set of triplet lenses and refocused on the entrance slit (H: 13 mm \times W: 10 μm) of the spectrograph (IsoPlane SCT 320, Princeton Instruments, USA) by another triplet lens. The focusing lens and a 90degree turning mirror placed in between the lenses were mounted on a linear motorized stage (MTS50-Z8, Thorlabs Ltd., UK). The moving stage allows implementing the push-broom acquisition in the spatial x-dimension by scanning the image horizontally across the spectrograph slit. The 300 grooves per mm grating was used for collecting spectral datacubes at

280-409 nm, 394-523 nm, 582-711 nm, and 677-806 nm, where a high-pass glass filter (cut-off wavelength at 500 nm) was added for the last two wavelength windows to minimize the interference from the 2nd order dispersion. The 1800 grooves per mm grating was used to collect at 363-381 nm (N2 second positive system, $C^3 \prod_u -B^3 \prod_g$) and 378–396 nm (N_2^+) first negative system, $B^2 \sum_{u}^{+} -X^2 \sum_{g}^{+}$.

The spectrograph features an ICCD camera (iStar 334T, Thorlabs Ltd., UK, 1024×1024 pixels, pixels size of 13×13 μ m), with no binning, cooled to -20 °C for all the acquisitions. An exposure of 0.1 s was used for the 280-409 nm and 394-523 nm windows, while for the other four windows, 15 on-chip accumulations with 0.1 s gate duration were applied to compensate for the lower intensities observed. A homemade LabVIEW program allowed the automation of the Pb-HSI acquisition¹⁷ while the hyperspectral information was analyzed and displayed by ImageJ²¹ and MATLAB 2018a.

Sub-pixel shifting

The SPS process is a deconvolution method utilized to turn a series of low-resolution images into a high-resolution image by using a higher sampling rate.22,23 The implementation and optimization of the SPS to the Pb-HSI was discussed in previous work.17 The acquisition SPS parameters were set as: spectrograph entrance slit width = 10 μ m, motor scan step width = 2 μ m, leading to a deconvolution factor of 10/2 = 5, and the cutoff frequency of the lowpass noise filter was 0.15.

Abel's inversion

Abel's inversion is a mathematical protocol that allows for converting the convoluted LOS information to the deconvoluted radially resolved distribution when cylindrical symmetry conditions exist.24 The optimized DFT-based Abel's inversion reconstruction method implemented here was previously developed for SPS Pb-HSI.18 The reconstruction parameters used in this study were: 3D median noise filter with 3-pixel radius, number of cosine expansions in the Fourier-transform was set to 8, and number of pixels in radial dimension (limited by the image acquisition) set to 100.

Atmospheric pressure dielectric barrier discharge

A μDBD discussed in previous work was used as the emission source.17 The inter-electrode distance was set to 6 mm. The power-electrode was placed closer to the capillary tip at a distance of 5 mm. The effluent of the plasma made direct contact with the surface of a sample fixed on an independent X-Y-Z stage (Model A, Line Tool Co. USA) with a capillary tip-tosample distance set to 1 mm. In this study, a low-density polyethylene (LDPE, 0.92 g cm⁻³, melting point: 110 °C, Boedeker Plastics Inc., USA) block and a copper block (99.9% purity, Multipurpose 110 Copper, McMaster-Carr, USA) were used as model samples. The helium discharge gas (99.999% purity, Ultra High Purity 5.0 Grade Helium, Airgas, USA) flow rate was varied from 0.1 to 0.4 L min⁻¹ by a mass flow controller (EW-32907-67, Cole-Parmer, USA). The plasma was powered by an alternating current (AC) generator (PVM500, Information

Unlimited, USA) with a frequency of 30 kHz and applied voltage varied from 6 kV to 8 kV.

Electrical characterization

The applied voltage and frequency were measured with an oscilloscope (DSOX3034A-Digital Storage Oscilloscope, Agilent Technologies, USA) through a high-voltage probe (1000:1 attenuation, P6015A High-Voltage Passive Probe, TEKTRONIX, USA). The current was calculated through the measured potential drop over a 1 k Ω resistor (10:1, N2863B Oscilloscope Probe, Agilent Technologies, USA). A nitrogen displacement gas was used instead of the helium plasma gas to achieve a higher breakdown voltage and ensure no plasma was generated during displacement current measurements. The nitrogen displacement gas (99.999% purity, NI 300 UHP, Airgas, USA) was introduced independently into the μ DBD through a stainless-steel T-piece union fitting (SS-400-3, 1/4 inch tube OD., Swagelok, USA) with a flow rate ranging from 0.1–0.4 L min $^{-1}$.

Determination of plasma temperatures

Vibrational temperature. $T_{\rm vib}$ is an important property used in plasma diagnostics. For example, in nitrogen-containing plasmas, *i.e.* ambient dielectric barrier discharges, the inelastic collision between the free electrons and the nitrogen is very efficient and the $T_{\rm vib}$ very rapidly equilibrates with the $T_{\rm e}$. ¹³ The Boltzmann plot is a well-established method for the determination of the plasma temperature through the relative line intensities. According to the Boltzmann law, the number of molecules excited to certain vibrational states is proportional to ${\rm e}^{-\frac{E_{\rm v}}{k_{\rm B}T}}$, where $E_{\rm v}$ is the vibrational energy, and it has the following relationship with band intensities: ^{12,26}

$$I_{v',v''} = Cv^4 A(v',v'') e^{-\frac{E_v}{k_B T}}$$
 (1)

or

$$\ln\left(\frac{I_{v',v''}}{v^4 A(v',v'')}\right) = -\frac{1}{k_{\rm B}T} E_{\rm v} + C \tag{2}$$

where C is an experimental constant, ν' is the vibrational quantum number of the upper state, ν'' is the vibrational

quantum number of the lower state, $A(\nu',\nu'')$ is the transition probability, and ν is the wavenumber of the band head, $k_{\rm B}$ is the Boltzmann constant, and T is the temperature. Here in this study, the second positive system of the N₂ transition (C $^3\Pi_{\rm u} \rightarrow$ B $^3\Pi_{\rm g}$) is used to determine the $T_{\rm vib}$ of the plasma from the slope of the plot. Three band heads in the N₂ (C \rightarrow B) transition measured in the 363–381 nm window (1800 grating) are used for the Boltzmann plot: N₂(2 \rightarrow 4) at 370.9 nm, N₂(1 \rightarrow 3) at 375.4 nm, and N₂(0 \rightarrow 2) at 380.4 nm, respectively. The radially resolved emission is subsequently used to calculate the radially resolved $T_{\rm vib}$. Good linearity is shown in the plots with $R^2 > 0.99$.

Rotational temperature. The $T_{\rm rot}$ is another important fundamental parameter for plasma diagnostics, corresponding to the distribution of the molecular rotational states. A rapid equilibrium can be accomplished between the molecular rotational states and the translational energies of the molecules; therefore, it is commonly agreed that the T_{rot} is very close to the gas kinetic temperature $(T_g)^{28,29}$ Here, the T_{rot} was determined by fitting simulated spectra to the experimental spectra at selected positions in the radially resolved images. The experimental spectra are obtained from the rotational transitions of the $N_2^{\ +}$ first negative system (B $^2{\sum_u}^+\to$ X $^2{\sum_g}^+$) in 378–396 nm window (1800 grating). The wavelength range of interest is from 389.67 to 390.55 nm, which includes eight peaks of the R branches from K'' = 13 to K'' = 6 of the N_2^+ band.³⁰ The simulated spectra are computed using LIFBASE 2.1.1 (ref. 31) with a total resolution of 0.7664 nm (instrumental response and other broadening), pressure of 760 Torr in air, and a Voigt line shape with 15% Lorentzian. Fig. S2† shows the comparison between the experimental and simulated spectrums and the best-fit T_{rot} was determined by the lowest Chi-square value (χ^2) obtained.

Erosion crater characterization

The erosion crater shape and depth were measured by a non-contact optical profilometer (WYCO NT2000, Veeco, USA) based on a Mirau interference microscope. The phase-shifting interferometry mode (PSI) allowed the depth resolution of 0.1 nm with the height range <160 nm. The total scan region

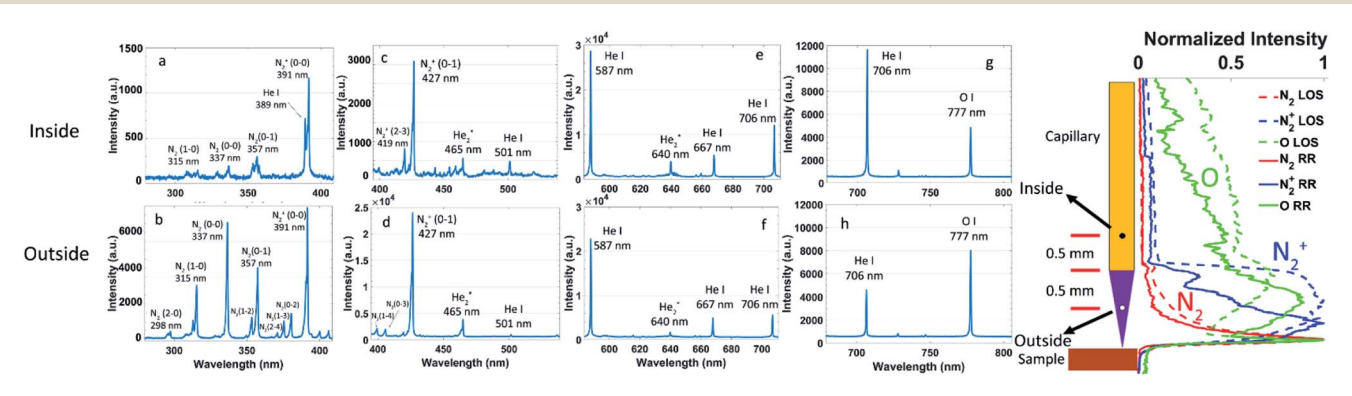


Fig. 1 Line-of-sight OES spectra measured at the axis position 0.5 mm inside the capillary (a, c, e and g), and 0.5 mm outside of the capillary (b, d, f and h). The applied voltage is 8 kV and the flow rate is 0.4 L min⁻¹. Note that ICCD conditions are different between distinct spectral windows. The image to the right shows plasma axial profiles of LOS vs. radially resolved spectral images.

was 1.236 \times 1.236 mm, and the detector is 736 \times 736 pixels. The lateral spatial resolution is limited by the 1.68 μ m pixel size. The data from the measurements were displayed and analyzed by the WYCO Vision 32 software and MATLAB 2018a.

Results

Line-of-sight optical emission spectra

It is instructive to look at the LOS spectral datacubes along the axial dimension to obtain an overview of the excited species.

Fig. 1 shows significantly different intensity distributions for selected spectral windows at the axial position 0.5 mm inside (Fig. 1a, c, e and g) or outside (Fig. 1b, d, f and h) of the capillary tip under the same plasma operating conditions. For example, in the 280–409 nm window inside the capillary (Fig. 1a) the $\rm N_2^+$ emission (391 nm) is most intense while the $\rm N_2$ bands are about an order of magnitude less intense. In contrast, the region outside the capillary (Fig. 1b) shows overall higher and comparable intensities for the $\rm N_2$ and $\rm N_2^+$ bands. It is also worth noting that a He I emission peak at 389 nm can be observed

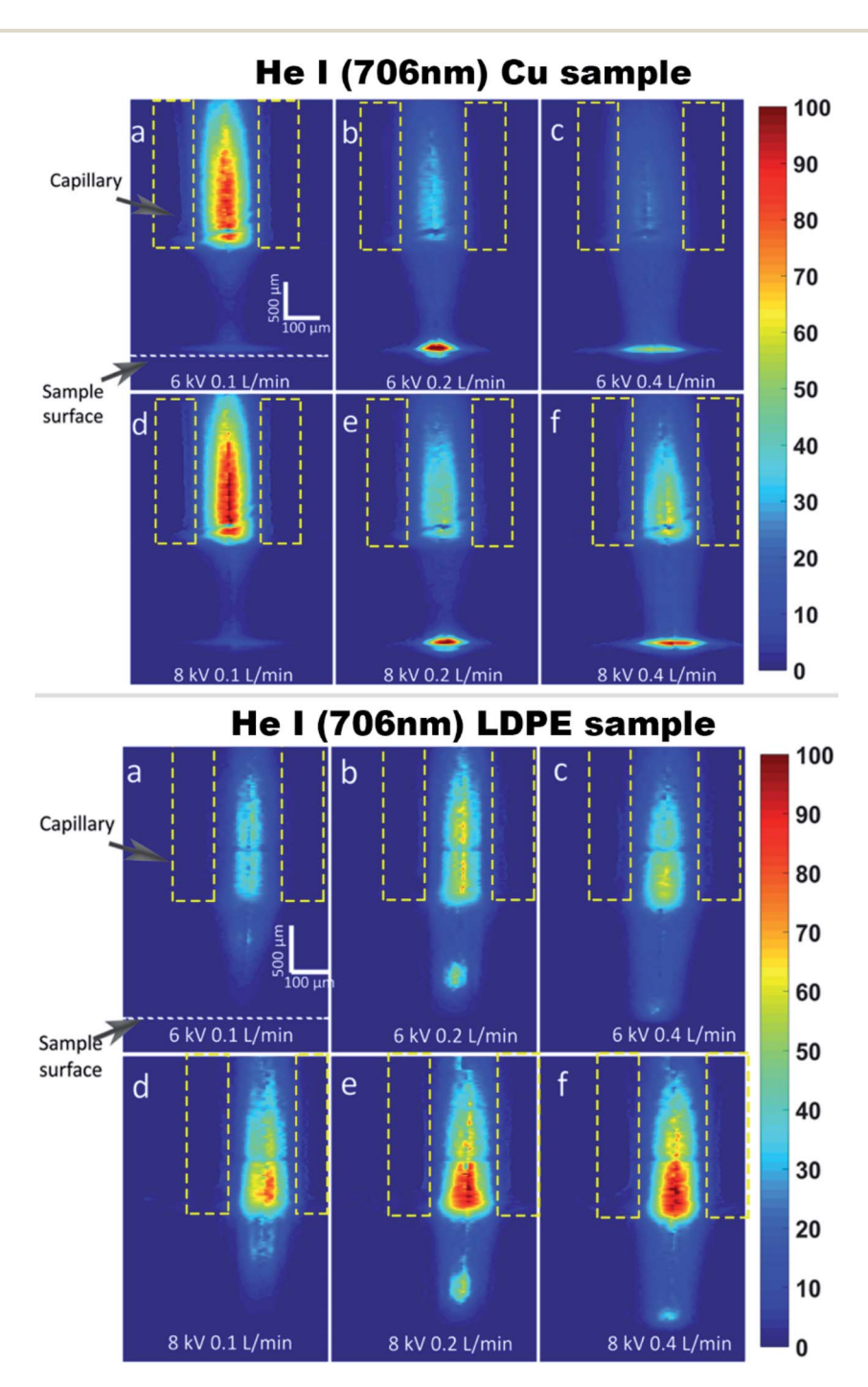


Fig. 2 Radially resolved He I (706.5 nm) optical emission intensity maps at varying applied voltage and plasma gas flow rate with a Cu sample (top) and LDPE sample (bottom).

Paper JAAS

inside the capillary but not outside. Another example of a similar trend is for the 677–806 nm window where the relative intensity ratio of the He I to O I is >1 inside the capillary but <1 outside of the capillary. These rough distributions show how the concentration of excited atmospheric species is higher outside the capillary and gives an indication of the energy transfer pathways between different plasma species that need to be studied in further detail.

Furthermore, the far right of Fig. 1 shows a comparison of the normalized axial OES profiles obtained from LOS νs . radially resolved (RR) images. The profile of N_2^+ is significantly different, where the radially resolved data shows the increase in intensity taking place closer to the sample surface compared to the LOS profile. This may indicate that some mechanisms of N_2^+ production may be more significant than previously considered, where only LOS axial profiles where available and used for proposing dominant mechanisms based on the spatial coincidence of increases/decreases in OES intensities from different species. This also illustrates the importance of obtaining radially resolved information, and that caution should be taken when deducing mechanism based only from LOS images.

Radially resolved optical emission intensity maps

Fig. 2 top shows the radially resolved distribution of He I emission at 706.5 nm, which populates the metastable ³P₂ triplet state ~ 20.97 eV (3s $^3S_1 \rightarrow 2p$ $^3P_{0,1,2}^{0}$), 33 under different plasma operating conditions. The dashed lines represent the position of the capillary and the Cu sample surface. In general, the radial distribution of He I emission shows a convex shape, which has the highest intensity in the axial position. Several emission distribution features can be observed when comparing different conditions. First, the distribution along the axis shows that the intensity is higher inside the capillary and decreases in the open-air region between the capillary tip and the sample surface at 0.1 L min⁻¹. However, the intensity increases rapidly again and reaches its maximum at the sample surface at 0.2 L min⁻¹, while maintaining a similar trend at 0.4 L min⁻¹ but with a less intense peak at the sample surface. Second, the overall intensity is slightly higher under the same flow rate when the applied voltage is increased from 6 kV to 8 kV. Third, the intensity inside the capillary decreases significantly (\sim 50%) when the flow rate is increased from 0.1 L min⁻¹ to 0.2 L min⁻¹. Note there is a very small region above the edge of the capillary tip where the emission intensity decreases that was confirmed to be a non-transparent feature outside the capillary and can also be observed at other wavelengths.

The bottom of Fig. 2 shows the radially resolved distribution of He I emission (706.5 nm) with the LDPE sample. Compared with the Cu sample, the most significant difference is the position of the second intensity maximum outside the capillary. For the Cu sample (Fig. 2 top), the second maximum is at the sample surface under all conditions studied, while for the LDPE it occurs further upstream and moves closer to the surface at higher flow rates. On the other hand, the relative intensity at the surface is much lower with the LDPE sample (Fig. 2 bottom). In addition, higher flow rates result in higher intensities inside the

capillary, in contrast to the opposite trend observed for the Cu sample.

Fig. S3† shows the radially resolved distribution of the He I emission (3d $^{3}D_{1,2,3} \rightarrow 2p \, ^{3}P_{0,1,2}^{\circ}$) at 587.6 nm with the Cu sample block as the substrate. This transition also populates the ³P₂ triplet state. These images show a similar pattern compared to the 706.5 nm, however, a major difference is observed inside the capillary, where the intensity is highest at the lowest flow rate for the 706.5 nm line, but it increases slightly with increased flow rate for the 587.6 nm line. Furthermore, Fig. S4† shows the radially resolved distribution of He I emission at 388.9 nm $(3p^3P_2 \rightarrow 2 \text{ s}^3S_1)$ with different plasma operating conditions, in the presence of the Cu sample. The emission images were obtained using the 1800 grating in order to enhance the spectral resolution, which allows the He I (388.9 nm) line to be resolved from the adjacent N_2^+ 0-0 first negative system around 391 nm. This transition populates the helium metastable atoms in the triplet state (19.82 eV).34 The intensity inside the capillary shows a clear trend of decreasing as the flow rate increases, while the intensity outside the capillary increases. Unlike the previous two emission species, the 388.9 nm line does not have the highest intensity at the plasma/sample interface. Another feature of the emission is that the intensity increases from 6 kV to 8 kV, both inside and outside of the capillary.

Fig. 3 shows the radially resolved distribution of N₂⁺ excited species, 0–0 first negative system (B $^2\sum_u^+ \rightarrow X ^2\sum_g^+$ transition) at 391 nm.35 In the case of the Cu sample (Fig. 3 top) it is evident that the N2+ has a much higher intensity in the open-air region between the capillary and the sample surface. The overall intensity increases along with both applied voltage and flow rate. A noticeable difference compared with the He I emission is that the N_2^+ has lower intensity at the axial position, in the region adjacent to the capillary tip. The resulting hollow-cone shape distribution surrounds the perimeter of the He I emission (cf. Fig. 2 top). It is evident that the increase of the flow rate promotes the outer layer of the hollow-cone shape to extend closer to the sample surface where a second intensity maximum appears. The trends with LDPE sample (Fig. 3 bottom) are very similar with the absence of the second intensity maximum at the surface.

Fig. 4 shows the radially resolved band head emission of excited N₂, 0-2 second positive system (C $^{3}\prod_{u} \rightarrow B ^{3}\prod_{g}$ transition) at 337 nm.35 In the case of the Cu sample (Fig. 4 top), for all the plasma operating conditions studied, the intensity of N₂ emission is very low inside of the capillary and it increases from the capillary tip towards the sample surface where it reaches its maximum. The region of highest intensity is larger when the applied voltage is increased from 6 kV to 8 kV under the same flow rate. When the flow rate increases, the radial profile changes from the convex-shape to the concave-shape, resulting in a hollow-cone distribution, similar to the one observed for the N_2^+ emission but with a larger outer radius. The maximum intensity at the sample surface peaks at 0.2 L min⁻¹ and decreases at 0.4 L min⁻¹, which is similar to the He I emission distribution (cf. Fig. 2). The trends with LDPE sample (Fig. 4 bottom) have some similarities, but significant differences are

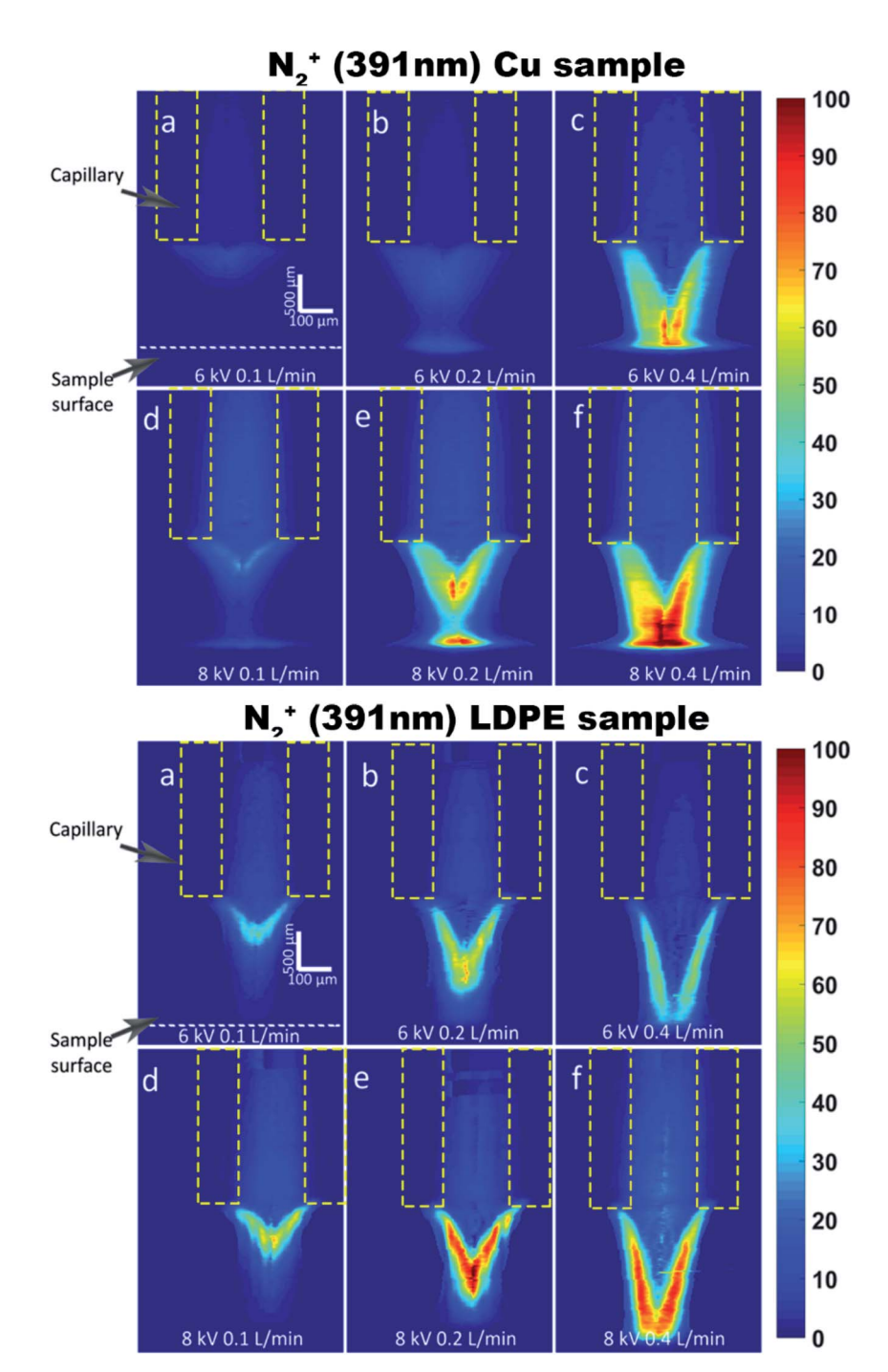


Fig. 3 Radially resolved N_2^+ (391 nm) optical emission intensity at varying applied voltage and plasma gas flow rate with a Cu sample (top) and LDPE sample (bottom).

also clear, such as the hollow-cone shape being evident at the lowest flow rate and applied voltage, as well as the absence of the second intensity maximum at the sample surface.

Fig. 5 shows radially resolved OES maps for the He $_2*$ band head at 640 nm (d $^3\sum_u{}^+ \rightarrow b$ $^3\prod_g$ transition). In general, the intensity of He $_2*$ increases with both the applied voltage and flow rate, while there is a slight decrease at 6 kV from 0.2 L min $^{-1}$ to 0.4 L min $^{-1}$. It is also very clear that increasing the flow rate results in a greater intensity of the emission outside of the capillary extending into the open-air region, with a second

maximum at the sample surface with higher flow rate. The main difference between samples is that the LDPE does not show the second intensity maximum at the sample surface.

Fig. 6 shows the radially resolved emission intensity distribution of atomic oxygen (($^4S^o$)3p $^5P_{1,2,3} \rightarrow (^4S^o)$ 3p $^5S_2^o$ transition) at 777 nm. 33 In general, the radial distribution of O I emission shows the highest intensity in the axial position and gradually decreases toward the edge of the plasma. In the case of the Cu sample (Fig. 6 top), the emission distribution is similar to the He I emission (*cf.* Fig. 2 top) and several features

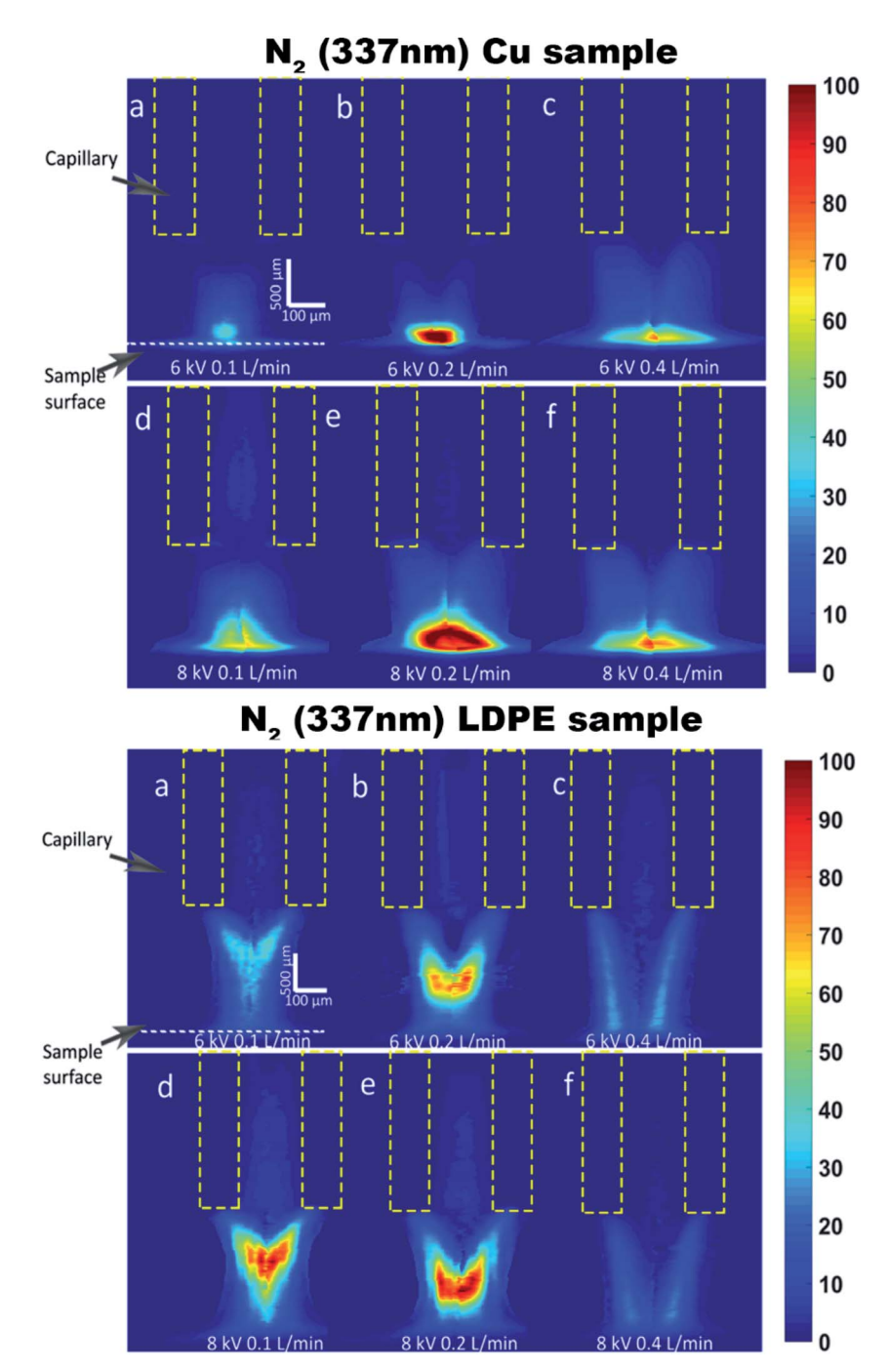


Fig. 4 Radially resolved N₂ (337 nm) optical emission intensity at varying applied voltage and plasma gas flow rate with a Cu sample (top) and LDPE sample (bottom).

can be observed. First, with a 0.1 L min⁻¹ flow rate, the lateral emission distribution along the axis is higher inside the capillary and it decreases in the open-air region between the capillary tip and the sample surface. Second, with 0.2 L min⁻¹ and 0.4 L min⁻¹ flow rate, the intensity increases rapidly again near the sample surface, where it reaches its maximum at 0.2 L min⁻¹, and then decreases at the highest flow rate. Third, the intensity inside the capillary decreases significantly (~55%) from 0.1 L min⁻¹ to 0.2 L min⁻¹. The O I OES maps are significantly different for the LDPE sample (Fig. 6 bottom). The maximum intensity is always outside the capillary and it extends further onto the sample with increasing flow rate. In addition, the intensity is always higher at increased applied voltage, and there is no maxima anchored at the sample surface.

Vibrational and rotational temperature

Fig. 7 top shows the radially resolved T_{vib} map calculated from Boltzmann plots of the N2 emission intensity maps under different plasma operating conditions. The uncertainty of the temperature is composed of two parts: the slope fitting error

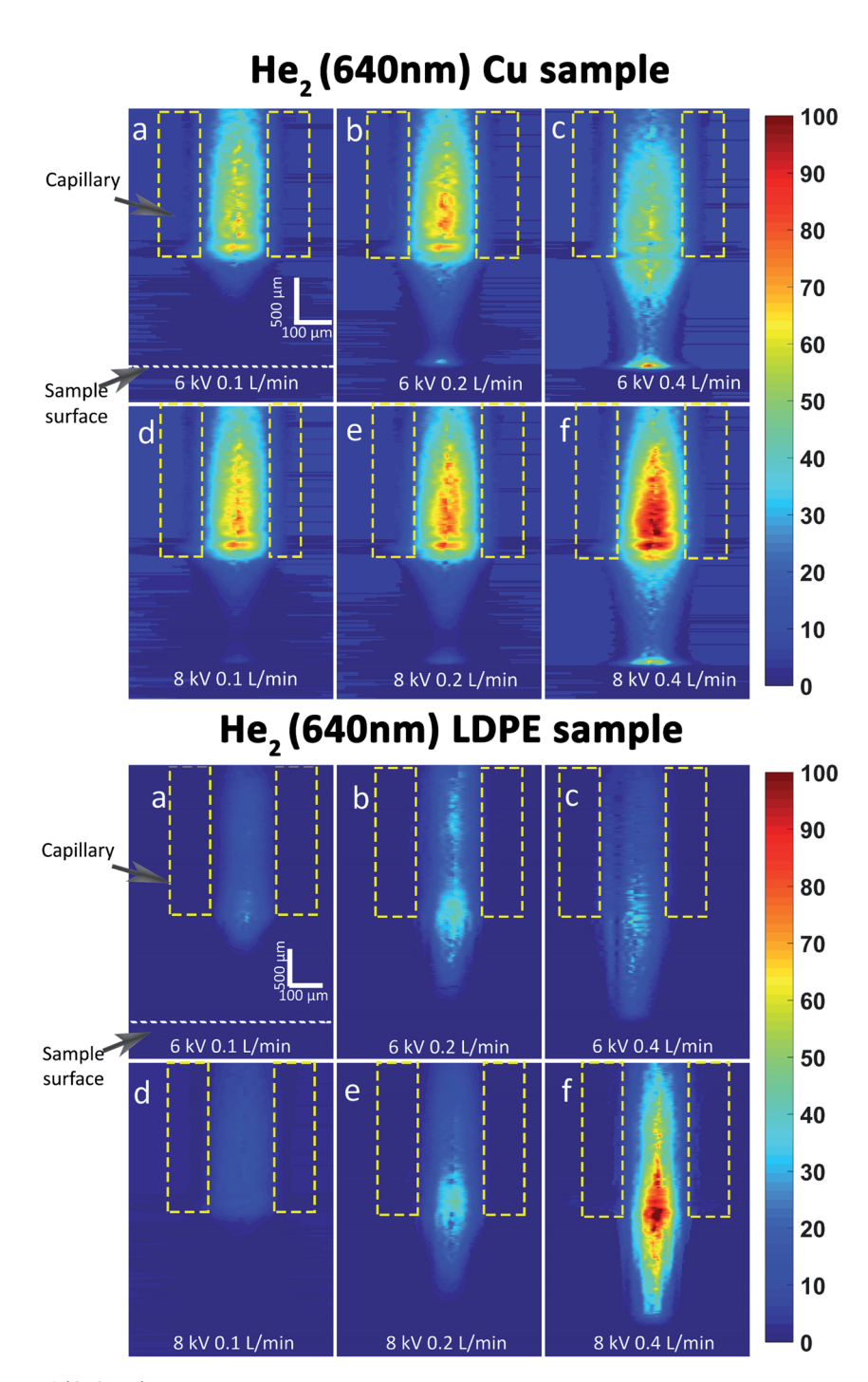


Fig. 5 Radially resolved He_2 * (640 nm) optical emission intensity at varying applied voltage and plasma gas flow rate with a Cu sample (top) and LDPE sample (bottom).

and the measurement precision. The propagated uncertainty in the calculated $T_{\rm vib}$ is <12%. The $T_{\rm vib}$ inside the capillary is \sim 1000 K with 6 kV applied voltage and 0.1 L min⁻¹ flow rate, and it increases with the voltage and flow rate. In contrast, the $T_{\rm vib}$ outside of the capillary can reach as high as 3000 K. It is observed that the $T_{\rm vib}$ maps show a cone-shape outside of the capillary, which extends further out as the flow rate increases. It is also worth mentioning that the temperature decreases rapidly to 500 K at the boundary of the cone shape.

Fig. 7 bottom shows the radially resolved $T_{\rm rot}$ maps with different plasma operating conditions. Note that the $T_{\rm rot}$ maps, as detailed in the Experimental section, were determined by fitting simulated spectra via LIFBASE software, which makes pixel-by-pixel calculation of the $T_{\rm rot}$ very time-consuming. Here, enough spatial positions were selected to construct a temperature map via a 2-dimensional linear interpolation algorithm, in an effort to keep a practical image processing time. The selected spatial positions are depicted by the grid-line intersection

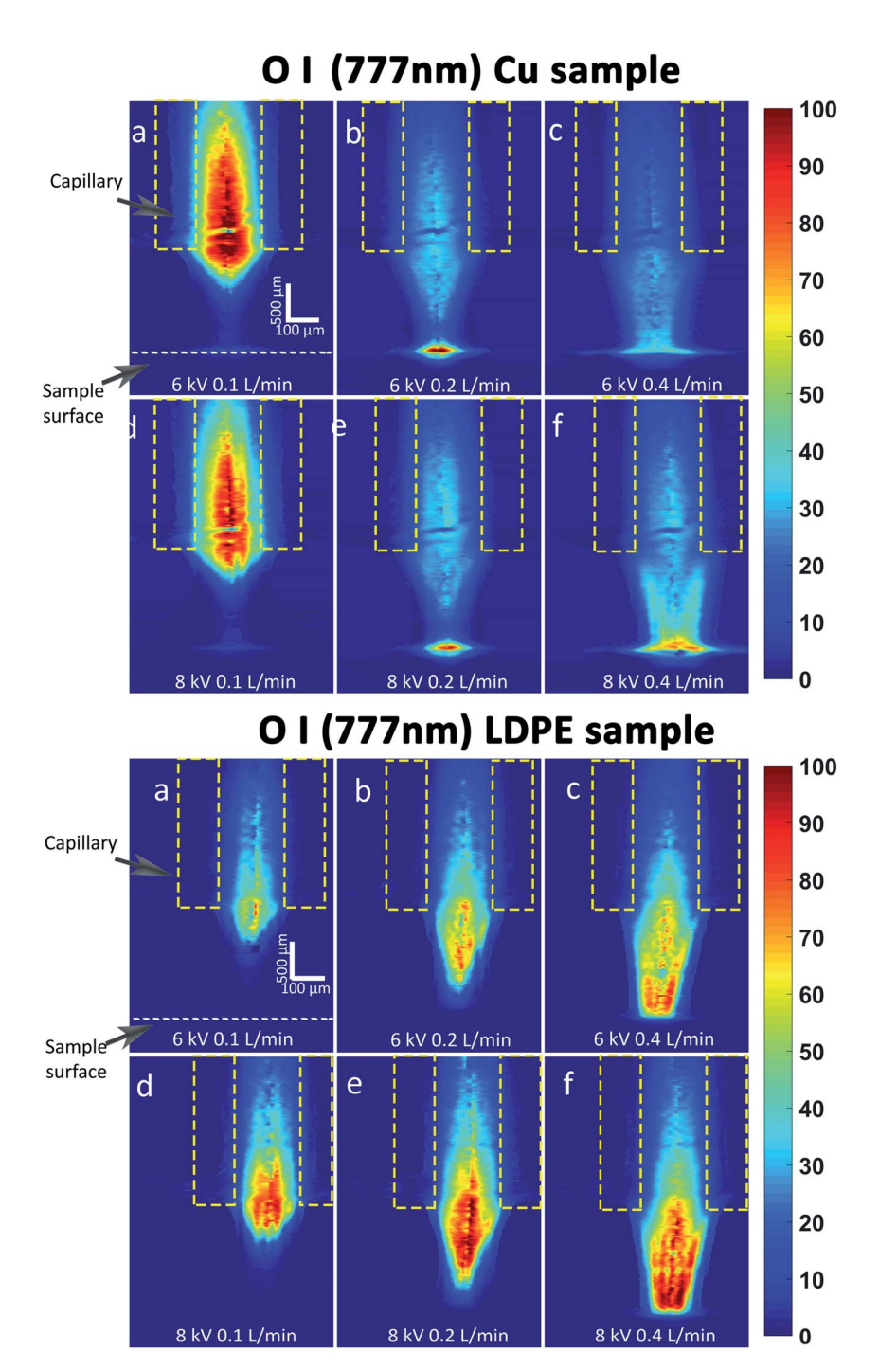


Fig. 6 Radially resolved O I (777 nm) optical emission intensity at varying applied voltage and plasma gas flow rate with a Cu sample (top) and LDPE sample (bottom).

points in Fig. 7 bottom. The uncertainty of the $T_{\rm rot}$ is composed of two parts: the fitting error of the software simulation and the measurement reproducibility. The RSD calculated from the Chisquare value (χ^2) between the experimental spectra and the simulated spectra is only ~0.5%, while the RSD of three replicate acquisitions is ~6.5%, which dominates the uncertainty of the $T_{\rm rot}$. The $T_{\rm rot}$ inside of the capillary is around 450 K at 6 kV and increases to about 550 K at 8 kV. At lower flow rates, $T_{\rm rot}$ decreases to about 350 K toward the tip of the capillary and then increases near the sample surface where it reaches a maximum

of \sim 700 K. As the flow rate is increased, the region of lowest temperature is enlarged and the maximum $T_{\rm rot}$ region is constricted toward the sample surface. In contrast, at the highest flow rate, 0.4 L min⁻¹, it is observed that the region of lower $T_{\rm rot}$ is extended even further all the way to the sample surface.

Electrical characterization

The current measured during plasma operation is the total current (I_{total}) which is composed of two parts: the current flow

JAAS

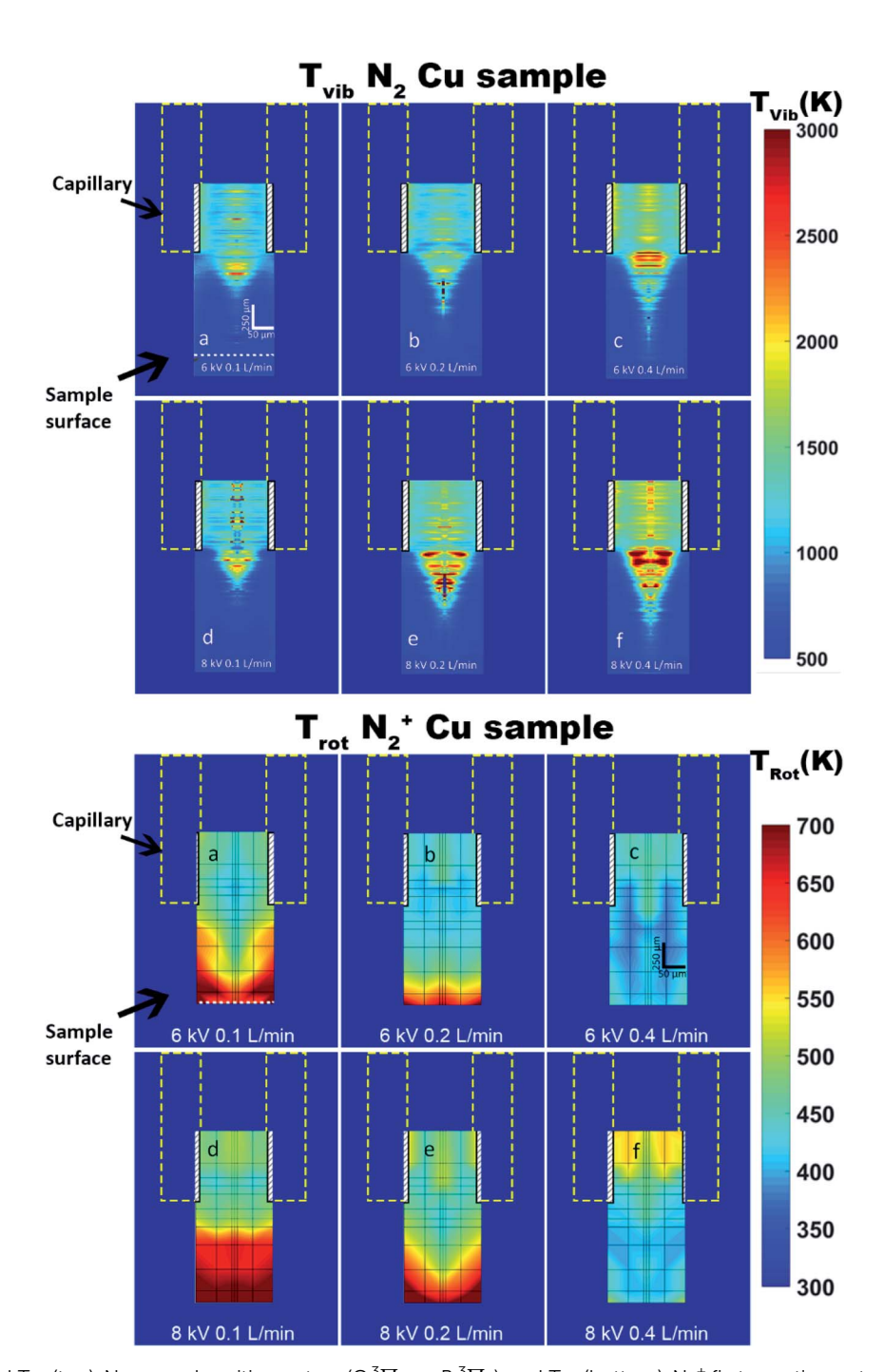


Fig. 7 Radially resolved T_{vib} (top), N_2 second positive system (C $^3\prod_u \to B^3\prod_q$), and T_{rot} (bottom), N_2^+ first negative system (B $^2\sum_u^+$) \to (X $^2\sum_q^+$), maps at varying applied voltage and plasma-gas flow rate. The Trot was determined by LIFBASE software fitting of the spectra measured at the cross points of the grid lines and interpolated

through the discharge and the current flow through the dielectric.25 The displacement current (Id) represents the current that flows through the dielectric when a different gas replaces the discharge gas and there is no active plasma present. The discharge current, or the conductive current (I_c) , can be calculated by the following equation: $I_c = I_{total} - I_d$.

Fig. 8A shows a selected conduction current waveform, calculated from the plasma total current and the displacement current waveforms. The single discharge peaks shown in each

positive and negative cycle indicate the plasma is in homogenous mode that leads to a more even/diffuse distribution of the discharge species, as opposed to a filamentary mode where the plasma species would be concentrated in different filament channels that would manifest as many random current peaks distributed along the waveform.³⁶⁻³⁸ Fig. 8B and C show how the conduction current, both RMS and peak-to-peak, increases with the applied voltage and flow rate.

Paper JAAS

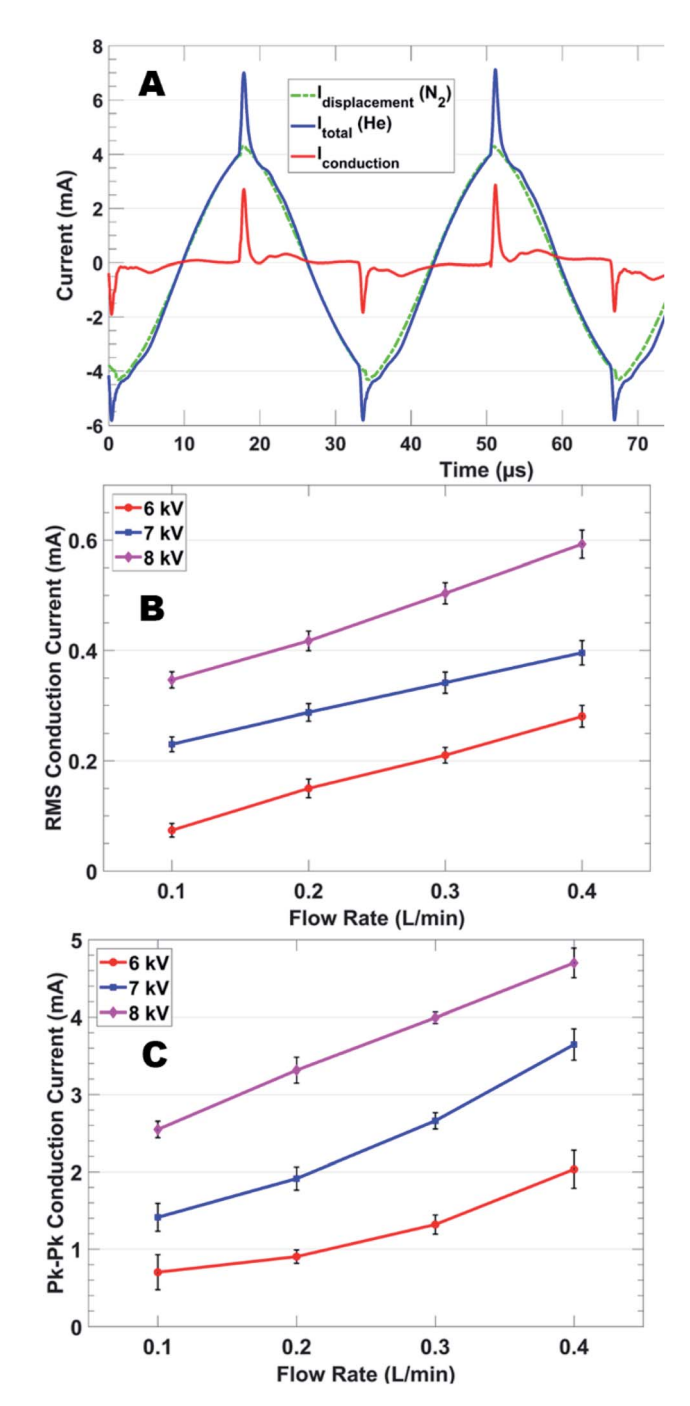


Fig. 8 (A) The conduction current of the plasma was calculated by subtraction of displacement current (nitrogen gas, no discharge) from the total current (discharged with helium gas), shown for 8 kV and 0.4 L min $^{-1}$. (B) The RMS and (C) peak-to-peak conduction current as a function of flow rate at different applied voltages.

Crater profilometry

Crater measurement. Fig. 9a shows the profilometry image of the Cu sample surface in contact with μDBD after 10 min with 8 kV applied voltage and $0.4~L~min^{-1}$ helium flow rate. It is clear that a crater is created on the surface, indicating not only desorption, but also erosion occurs on the Cu sample. Notice

that the crater bottom is higher than the surrounding positions, showing a convex shape crater.

In contrast, a much larger but shallower crater is formed on the LDPE surface under the same plasma operation conditions, shown in Fig. 9b. Based on the $T_{\rm rot}$ being >500 K at the LDPE surface (calculated in the previous section), the large crater area is most likely due to be by heat transfer from the plasma since the LDPE starts softening after 350 K. Fig. 9c shows the radially averaged cross-section profile of the crater. It is evident that the crater shows a convex shape at the bottom (blue line) with 0.4 L min $^{-1}$ flow rate. However, the convex shape does not exist in other flow rates, *i.e.*, a concave shape bottom (red line) crater is formed with 0.3 L min $^{-1}$. The possible explanation of the shape of the crater formation will be discussed in the following sections. The full-width at the top, the full-width at half-maximum, and the width at the convex shape bottom (shown in Fig. 9c) will be used in the discussion.

Crater shape vs. OES images. The plasma-sample surface interaction study is performed via the correlation between the crater shape and the radially resolved OES images. All the emission profiles are extracted at 52 µm (4 pixels) above the sample surface. Fig. 10a shows the comparison of full-width of the emission of 5 different plasma species and the full-width at the top of the crater, when the applied voltage is 6 kV. It shows that the N₂⁺ emission has the best correlation with the crater full width, with a percentage difference of 4% after averaging all 4 flow rate conditions. The N2 shows similar trends at 6 kV, with a larger diameter and an average difference of 32%, while the percentage is 39% for He I, 28% for O I, and 35% for He₂. A similar correlation relationship can be observed with 8 kV applied voltage (Fig. 10b). The average difference is 6% for N_2^+ emission, 16% for N2 emission, and 45-65% for other emissions. As mentioned in the Crater characterization section, the crater shows a convex-shape bottom when the flow rate is 0.4 L min⁻¹. Therefore, the FWHM of the emission profiles were also compared with the full width of the convex bottom in Fig. S5.† There is a similar trend of the emission FWHM of nitrogen species with the crater full width, albeit not as clear as with the emission full width.

Discussion

Capillary tip and open-air region

It is commonly believed that the generation of the He atoms excited to metastable levels (19.8 eV or 20.6 eV, denoted He_m), or to a higher excited state (>20.6 eV, denoted He*), is through the electron-impact mechanism, 33,34

$$e^- + He \rightarrow e^- + He_m$$
 (3)

$$e^- + He \rightarrow e^- + He^* \tag{4}$$

and the metastable states have a lifetime in the order of seconds, allowing ionization to occur efficiently.³⁹ There are several main routes for the loss of excited helium species with major products of He⁺, He₂⁺, and He₂*:

Metastable-metastable ionization:40,41

JAAS Paper

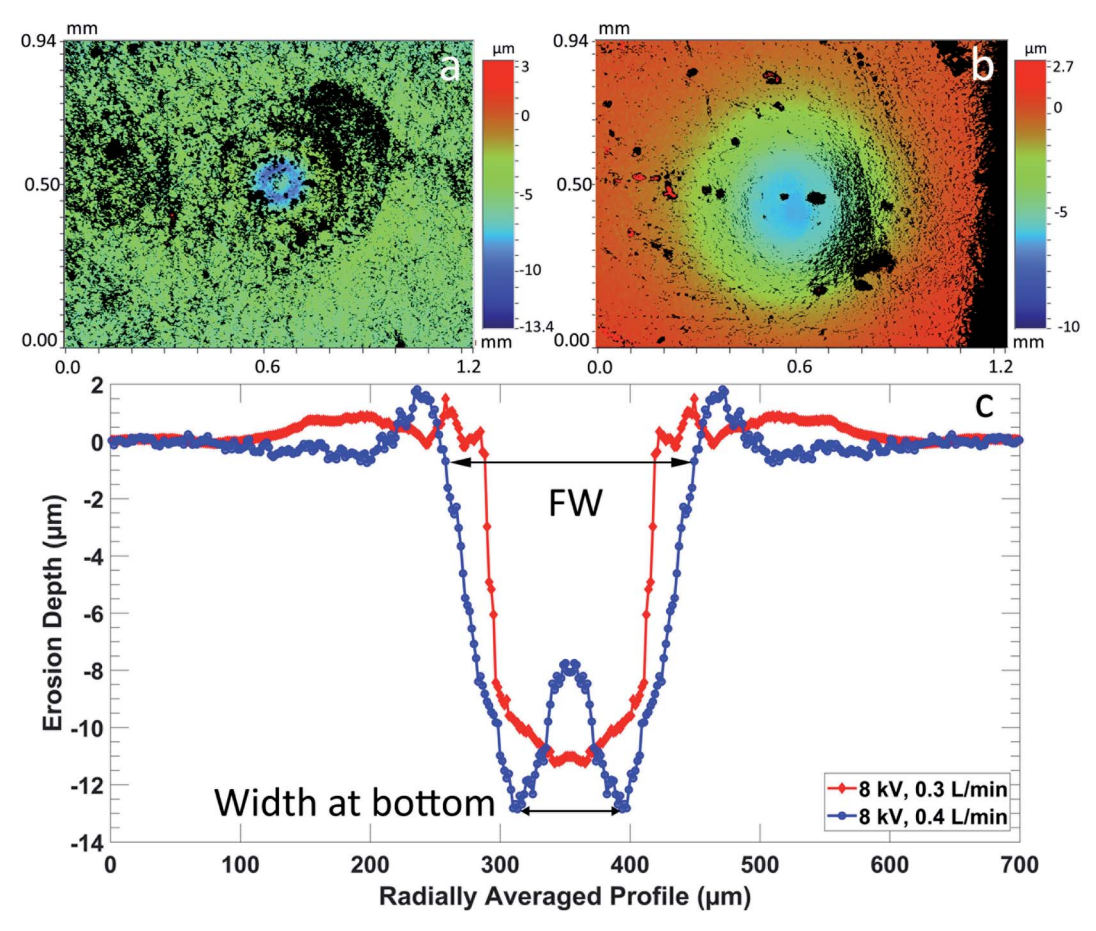


Fig. 9 Profilometry images of (a) Cu sample and (b) LDPE sample. (c) Radially averaged cross-section profile of the Cu sample under different flow rates.

$$He_m + He_m \rightarrow He^+ + He + e^- (k = 8.7 \times 10^{-16} \text{ m}^3 \text{ s}^{-1})$$
 (5)

Metastable-metastable associative ionization: 40,41

$$He_m + He_m \rightarrow He_2^+ + e^- (k = 2.03 \times 10^{-15} \text{ m}^3 \text{ s}^{-1})$$
 (6)

Metastable induced association:42

$$\text{He}_{\text{m}} + 2\text{He} \rightarrow \text{He}_{2}^{*} + \text{He} (k = 1.9 \times 10^{-46} \text{ m}^{6} \text{ s}^{-1})$$
 (7)

Hornbeck-Molnar associative ionization:43

$$\text{He}_{\text{m}} + \text{He} \rightarrow \text{He}_{2}^{+} + \text{e}^{-} (k = 1.5 \times 10^{-17} \,\text{m}^{3} \,\text{s}^{-1})$$
 (8)

It is important to take into account the plasma species' residence time in the imaged region. Based on the gas linear velocity (flow rate: 0.1 to 0.4 L min; capillary i.d.: 150 μm), which is in the range of $\sim\!100$ m s $^{-1}$ to 400 m s $^{-1}$, it would take $\sim\!2.5~\mu s$ to 10 μs for the plasma species to traverse this 1 mm region. However, under the 30 kHz AC power conditions used here, there is an ionization wave at each cycle that is faster, for example touching the sample substrate within 10 s of ns as reported in ref. 44. The excited He I species have a very short lifetime and reported energy exchange with other species on the order of $\sim\!50$ ns, which is several orders-of-magnitude shorter

than the residence time. Thus, the He I optical emission distributions measured here (Fig. 2, 706.5 nm; Fig. S3,† 587.6 nm, and Fig. S4,† 388.9 nm) are likely to contain contributions that are representative of regional excitation processes.

All the He I optical emission maps show a general decrease in intensity inside the capillary, along with higher intensity in the region between the capillary and the sample surface, as the flow rate is increased. It is possible that the higher linear velocities allow the excited species just inside the capillary to travel further downstream before relaxing radiatively. In addition, a larger number density of higher energy electrons may be available further downstream at higher flow rates, such that electron impact excitation (eqn (3)) can take place more efficiently. This is supported by the measured distribution trends of T_{vib} (cf. Fig. 7, given that these N_2 transitions typically arise from electron impact processes and are thus indicative of $T_{\rm e}$), where the cone-shaped tail region of higher T_{vib} extends further outward and displays higher temperatures at increased flow rates. Furter et al. 45 also measured a rise in the $T_{\rm vib}$ at increased voltages or flow rates on a larger sized DBDI source than used here (2 mm o.d.). Furthermore, all the He I transitions measured here populate metastable states, which would indicate that the He metastable number density surges further downstream from the capillary as the flow rate is increased.

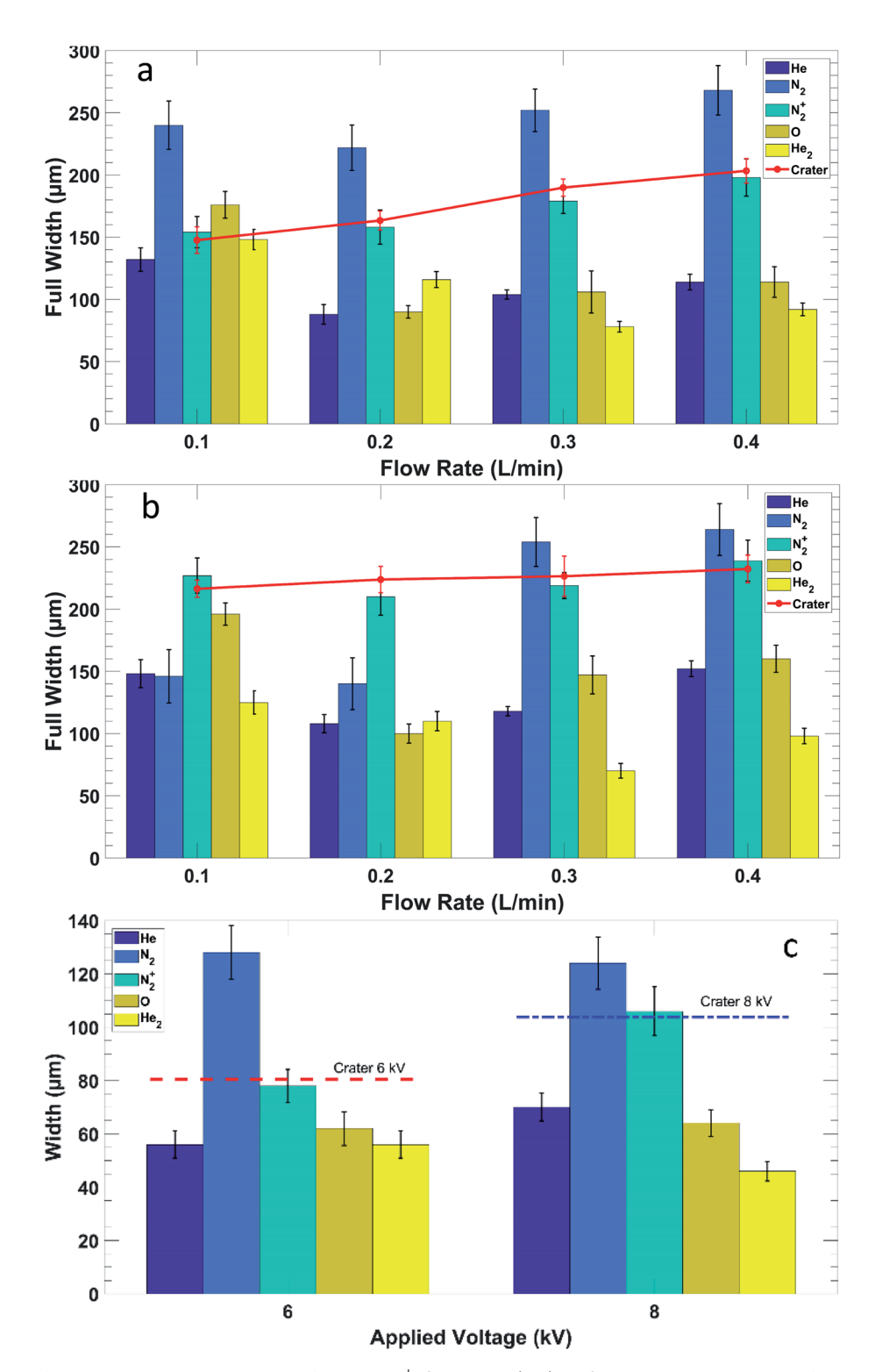


Fig. 10 The full width of the radially resolved emission of He, N_2 , N_2^+ , O, and He₂ (bar) at 52 μ m above the sample surface, compared with the full width at the top of the erosion crater (red line) from 0.1 to 0.4 L min⁻¹ flow rate. The applied voltage is (a) 6 kV and (b) 8 kV. (c) The FWHM of the emission are compared with the full width of the convex crater bottom with 0.4 L min⁻¹ flow rate, and 6 or 8 kV voltage applied, respectively. The error bars represent the standard deviation of the triplicate measurements.

This agrees with studies by Farnsworth *et al.* where the He metastable density in an APPJ, measured *via* laser-induced fluorescence (LIF), is reported to rise further away from the capillary tip as the flow rate is increased.⁸

Also, it is interesting to note that the radially resolved imaging allows the observation of the cone-shaped tail formed by the He I optical emission being followed downstream by the hollow cone-shaped optical emission of the N_2^+ (cf. Fig. 3). The

JAAS

nitrogen molecular ion $(N_2^{\ +})$ plays an important role in APPJs flowing into air, as it is generally agreed that $N_2^{\ +}$ is responsible for the formation of the protonated water clusters, which are known ionization reagents of interest. 46-48 Qayyum $et\ al.$ reported that the transitions related to the $N_2^{\ +}$ first negative system (B $^2\sum_u^{\ +}\to X$ $^2\sum_g^{\ +}$ transition) cannot be initiated in a pure nitrogen plasma at atmospheric pressure. However, the transition is almost resonant in the helium-based ambient ionization source. 49 There are three major reaction routes for the $N_2^{\ +}$ formation from the neutral ambient nitrogen gas. First,

$$\text{He}_{\text{m}} + \text{N}_2 \rightarrow \text{He} + \text{N}_2^+ + \text{e}^- (k = 7.11 \times 10^{-11} \text{ m}^3 \text{ s}^{-1})$$
 (9)

Second, via charge transfer (CT) with the helium dimer ion: 46,51

via Penning ionization (PI) with the helium metastable 48,50

$$\text{He}_2^+ + \text{N}_2 \rightarrow 2\text{He} + \text{N}_2^+ (k = 1.3 \times 10^{-9} \text{ m}^3 \text{ s}^{-1})$$
 (10)

Third, via direct electron excitation with high-energy electrons. It is possible to perform the ionization and excitation at the same time through a one-step process:⁵²

$$N_2 (X^{-1} \sum_{g}^{+}) + e^{-} (E > 18.7 \text{ eV}) \rightarrow N_2^{+} (B^{-2} \sum_{u}^{+}) + 2e^{-}$$
 (11)

Or it may go through the ionization and excitation separately with a two-step process:⁵³

$$N_2 (X^{-1} \sum_{g}^{+}) + e^{-} (E > 15.5 \text{ eV}) \rightarrow N_2^{+} (X^{-2} \sum_{g}^{+}) + 2e^{-} (12)$$

$$N_2^+(X^2\sum_g^+) + e^-(E > 3.2 \text{ eV}) \rightarrow N_2^+(B^2\sum_u^+) + e^-$$
 (13)

The spatial coincidence of the He I emission profile upstream and the N₂⁺ emission profile downstream indicates that PI plays an important role, as reported by Chan et al.32 for a larger DBD under typical desorption/ionization conditions, given that the He I transitions measured populate metastable states. This is further supported by the measured $T_{\rm rot}$ distribution (cf. Fig. 7). PI (eqn (9)) and CT (eqn (10)) reactions can produce excited nitrogen molecular ions, but the population of the resulting rotational states are different, which manifests as different T_{rot} . It is reported that the PI pathway can yield a rotational temperature of 360 \pm 30 K, while the CT pathway can yield 900 \pm 60 K.^{54,55} Therefore, at lower flow rates, the lower temperature region observed just outside the capillary is indicative of PI, while the much higher temperature region closer to the sample surface is indicative of CT. Moreover, increases in flow rate result in the higher temperature region shrinking toward the sample surface until it disappears at the highest flow rate, which correlates with the higher intensities of the He I optical emission (transitions into He metastable states) increasing toward the sample surface at higher flow rates. It is interesting to note that while the T_{rot} decreases with flow rate, the intensity of the N₂⁺ band head at 391 nm increases, showing a surge in excited N_2^+ , even when the concentration of N_2 from air diffusing into the same area should be lower. This is not just a shift in the populated levels, as indicated by the T_{rot} , because the spatial profile of the N_2^+ optical emission and the $T_{\rm rot}$

changes do not coincide (cf. Fig. 3 and 7, 8 kV and 0.2 L min $^{-1}$). It is worth noting that the plasma gas used, He UHP, does have a reported N_2 impurity content of 5 ppm, according to the manufacturer. It is also interesting to note that an increase of applied voltage or flow rate will lead to an increase of the plasma conduction current (cf. Fig. 8), suggesting that there will be more charged species present in the plasma. This correlates well with the trends of the N_2 ⁺ band head emission at 391 nm.

Plasma plume/surface interface

In the absence of a nearby sample surface, the N_2 optical emission peak appears just downstream of the N_2^+ (Fig. S7†), which confirms the results of Chan *et al.* for a larger DBD under typical ambient mass spectrometry conditions.³² Here, the radially resolved imaging allows the observation of the axial and radial structure of this sequence when the μ DBD plasma plume is exposed to the isolating LDPE sample surface (*cf.* Fig. 3 and 4). It is also evident that a full cone-tail shaped N_2 optical emission is observed at lower flow rates and is pushed closer toward the sample surface as the flow rate is increased, until the tip is no longer observed, but only the edges. The spatial distribution relationship between the excited N_2 and the N_2^+ suggests that the energy of the excitation is likely to come from a recombination mechanism with the excited nitrogen ion species, as proposed in ref. 32 and 56:

$$N_2^+ + e^- \rightarrow N_2^* (k = 3.5 \times 10^{-7} \text{ m}^3 \text{ s}^{-1})$$
 (14)

On the other hand, a very significant difference is observed in the N₂ optical emission distribution when the plasma plume is exposed to the copper sample, where the maximum intensity is always at the sample surface regardless of the voltage/flow rate settings. In fact, the optical emission of every plasma species imaged here displays a peak at the plasma/copper sample interface, particularly as higher voltages and flow rates. In contrast, exposing the plasma plume to the LDPE sample does not result in such emission peaks at the surface. The plasma optical emission spatial structure is pushed outward at higher flow rates but seems to be cut-off, or extinguished, at the LDPE surface. This phenomenon shows that the sample surface nature plays a critical role in the underlying mechanisms and is not just a passive component, which is of great significance toward plasma-based ambient desorption/ ionization applications. These differences may arise from several factors, including the polymer additives and fragments interacting with the plasma plume. Another significant difference is that the LDPE is an isolating surface, while the copper, even when it is not grounded but floating, presents a much more efficient charge reservoir/well.

Some effects of exposing the plume of an APPJ to a nearby surface have been previously described. For example, Farnsworth *et al.* showed that the presence of a glass slide surface 10 mm downstream of a He DBD resulted in an increase of the measured He metastable population at 4 mm downstream. This agrees with the results here, where exposing the plasma plume to the LDPE sample resulted in an emission peak of the He I (706.5 nm), which populates a metastable state, between the sample surface

and the capillary tip (cf. Fig. 2). Zaplotnik et al. measured the 2^3S_1 He metastable density in the plume of a single electrode APPJ and found that it increased up to $10\times$ in the presence of a sample surface, which also correlates with its conductivity.⁵⁷ In addition, they showed the He metastable density increased at a Fe sample surface placed 1–5 mm downstream. This also agrees with the He I optical emission image at 388.9 nm observed here, which populates the 2^3S_1 He metastable level, that peaks at the copper sample surface (cf. Fig. S4†), as well as the other He I transitions measured (cf. Fig. 2 and S3†).

Kushner et al. performed plasma hydrodynamics modeling, nonPDPSIM, on a He/O2 (99.8/0.2) APPJ, flowing into humid air and impinging on a thin varying dielectric ($\varepsilon/\varepsilon_0 = 2$, similar to LDPE, to 80) or metallic surface.44 It is worth noting that in their model the APPI was pulsed at 80 ns and their results are temporally resolved. They note that the ionization wave (IW), propagating from the APPJ onto the surface, is faster in the case of the metal substrate and it yields a higher T_e and n_e , as well as ion density. They also report an increase in the densities of certain neutrals, e.g. excited He I (including 2³S metastables) and excited N2, in the metal surface case, while citing the charging of the lower ε_r dielectric surface as partly responsible for their lower reported densities of excited neutrals. They observe the metal surface causing a return stroke that sustains the discharge for a longer time after the IW first impacts the surface. On the other hand, the dielectric surfaces promote the formation of surface ionization waves (SIW) radiating outward from the plasma axis, as a consequence of the fast surface charging and the horizontal electric field component that sustain them, along with a fast decrease of the vertical electric field component. Sobota et al. measured the T_e and n_e via Thomson scattering, as well as the densities and temperatures of O₂ and N₂ via Raman scattering, on a He APPJ (6 kV, 1 μs unipolar positive pulses at 5 kHz) flowing into air while exposing the plume to various target surfaces.⁵⁸ They report a significant rise in n_e (\sim 30% to 300%) and T_e (\sim 20% to 200%) just above the target (glass < water < copper), compared to the free-flowing plume case, during the start of the power pulse (-20 ns to +130 ns). Furthermore, in the case of the copper target, they were able to measure larger increases in n_e and T_e , as well as $T_{\rm rot}$ until 1.25 µs after the start of the power pulse. The authors report a diffuse discharge sustained above the copper target following the return stroke and propose that secondary electrons from ions impacting the surface are the source of electrons, taking into account that the copper target is floating.

Regarding the results herein, the peak in the He I optical emission intensities observed at the surface of the copper target indicate that more efficient electron impact excitation (eqn (3) and (4)) can take place in this region, supported by the higher $T_{\rm e}$ and $n_{\rm e}$ reported near the copper surface. It is highly probable that this is also the case for the other plasma species whose optical emission intensity peaks at the copper surface. It is particularly interesting for N_2 because in the case of the free-flowing plasma plume, excitation is mainly through recombination reactions, as discussed above (eqn (14)) and further indicated by the spatial sequence with N_2^+ optical emission. While this spatial coincidence is still there in the case of the

LDPE target, this is no longer the case at the copper target surface, which indicates that a different excitation mechanism of the N_2 state (C $^3\Pi_u$) is taking place, such as direct electron-impact excitation.⁵²

$$N_2 (X^{1} \sum_{g}^{+}) + e^{-} (E > 11.1 \text{ eV}) \rightarrow N_2 (C^{3} \prod_{u}) + e^{-}$$
 (15)

Excited helium dimer

Optical emission from the excited helium dimer $\mathrm{He_2}^*$, or excimer, is observed at 464 nm and 640 nm (ref. 59) (cf. Fig. 1c–f). Hill et al. reported that for the He dimer molecules, the singlet states are unstable with a radiative decay in several nanoseconds. However, the triplet state molecules are "metastable" with a radiative lifetime of seconds due to a strongly forbidden spin flip required for the radiative transition to the ground state of two free atoms. 61

Besides metastable induced association (eqn (7)), there are other proposed mechanisms for the generation of the excited helium dimer, for example, the dissociative recombination reaction of helium molecular ion:⁶²

$$\text{He}_2^+ + \text{He} + \text{e}^- \rightarrow \text{He}_2^* + \text{He} (k = 3.5 \times 10^{-27} \text{ cm}^6 \text{ s}^{-1})$$
 (16)

or the dissociative recombination reaction of helium He₃⁺ ion:^{63,64}

$$He_2^+ + He + He \leftrightarrow He_3^+ + He$$
 (17)

$$\text{He}_3^+ + \text{e}^- \rightarrow \text{He}_2^* + \text{He} (k = 3.4 \times 10^{-6} (T_e/80)^{-1.2} \text{ cm}^3 \text{ s}^{-1})(18)$$

Note that the presence of $\mathrm{He_3}^+$ has been detected in high-pressure discharges, but it is not a very stable molecule and eqn (18) is T_e dependent with a very fast reaction rate when the T_e is close to room temperature.³⁴

With respect to the role of He2*, it has been argued to be unimportant mainly from two aspects: first, the energy of He₂* is lower than the sum of the ionization and excitation energy of the N_2 (X $^1\Sigma_g^+ \rightarrow B ^2\Sigma_u^+$ transition, 18.7 eV) and secondly the number density of He2* are reported lower than Hem* in both vacuum65 and atmospheric66 environments. Nonetheless, the observations in this study indicate that He2* may play a more significant role than previously thought in the energy transfer pathways. First, according to eqn (12) and (13), the N² X $^{1}\sum_{g}^{+}$ \rightarrow $N_2^+ B^2 \sum_{u}^+$ transition can be accomplished in a two-step process if the energy requirement is met. The lowest triplet helium excimer He_2^* (a $^3\sum_u^+$) has an energy of 18.1 eV, 43 which is high enough for either ionization (15.5 eV) or excitation (3.2 eV) of N₂.⁵² Second, the results in Fig. 1 show that the emission intensity ratio of the He I (587.6 nm)/He₂*(640 nm) is less than 10 inside the capillary (Fig. 1e) but around 22 outside of the capillary (Fig. 1f), mainly from a decrease in He₂* intensity. The increase of the ratio suggests a higher helium excimer loss occurring, thus contributing to the energy transfer. Third, the radially resolved emission of He2* shows a similar distribution compared to He I, which correlates well to the distribution of N_2^+ .

Processes involving oxygen

Regarding the O I emission at 777 nm (cf. Fig. 6), it is important to note the differences when the plasma plume is exposed to a copper vs. LDPE sample. It is generally agreed that the atomic oxygen is dominant over molecular oxygen in the atmospheric pressure discharge due to the breakdown of the molecules in the plasma through electron-impact dissociation.⁶⁷

$$e^- + O_2 \rightarrow 2O^* + e^- (k = 7.1 \times 10^{-21} \text{ cm}^3 \text{ s}^{-1})$$
 (19)

Another possible pathway for atomic oxygen generation is through Penning ionization followed by dissociative recombination of ${\rm O_2}^+$ ions:⁶⁸

$$\text{He}_{\text{m}} + \text{O}_2 \rightarrow \text{He} + \text{O}_2^+ + \text{e}^- (k = 2.5 \times 10^{-10} \text{ cm}^3 \text{ s}^{-1})$$
 (20)

$$O_2^+ + e \rightarrow 2O^* (k = 4.8 \times 10^{-7} \text{ cm}^3 \text{ s}^{-1})$$
 (21)

In the case of the copper sample, electron-impact dissociation may play a more significant role, taking into account the similarities with the He I OES distribution and the higher $T_{\rm e}$ and n_e modeled in ref. 44 and measured in ref. 58, particularly at the plasma/sample interface. On the other hand, the LDPE sample would have much lower T_e and n_e , which would mean that Penning ionization would be a more significant mechanism. In addition, with the LDPE sample, it is interesting to note that the region of higher O I optical emission grows toward the sample surface as the flow rate is higher. This indicates that atomization/excitation mechanisms are significantly higher, because there is a lower amount of ambient air allowed to mix at higher flow rates, which would result in lower O2 concentrations in this region. It is important to also consider that atomic oxygen will diffuse faster compared to its molecular counterpart. In addition, it is worth noting that the plasma gas used, He UHP, does have a reported O₂ impurity content of 1 ppm, according to the manufacturer. In contrast, the copper sample has a higher O I optical emission intensity inside the capillary at the lowest flow rate, which changes to a peak found at the sample surface when using higher flow rates. In this case, however, another mechanism called helium channeling may be changing the O2 concentration originating from air, as reported for an APPJ impinging on metallic substrates,69 where the ion drag force results in a higher purity helium channel extending to the surface.

Furthermore, the oxygen may have an additional role in the resulting He metastable production. Winter et~al. showed the He metastable distribution in the plasma plume of a helium APPJ (axial pin electrode, $V_{\rm pp}$ 1.76 kV at 940 kHz AC) was significantly affected by the O_2/N_2 of the surrounding gas. To In short, the measured He metastable density was highest ($\sim 1 \times 10^{13}~{\rm cm}^{-3}$) with an 80% $O_2/20\%$ N_2 sheath gas composition, lower for 100% O_2 , significantly lower for 5% $O_2/95\%$ N_2 , and below their detection limit ($\sim 1 \times 10^{13}~{\rm cm}^{-3}$) for 100% N_2 . They observe similar trends when N_2 is replaced by Ar and attribute the lower He metastable density to the absence of O_2 , rather than the increase in N_2 . Kushner et~al. then used temporally resolved OES imaging with bandpass filters, for N_2 (390 nm

center, 20 nm FWHM) and He (707 nm center, 7 nm FWHM) species, as well as a plasma hydrodynamics computational model, non-PDPSIM, to study the effect of the surrounding gas composition in the same type of APPJ plume. They found that during the positive half cycle, the emission travels from the ambient air toward the jet nozzle, against the gas flow, when the shielding gas contains O₂. Their modeling results showed that when O₂ is in the shielding gas, an anion sheath surrounds the He channel and allows the IW to travel further, together with higher electric fields at the front, which results in the higher metastable density. Thus, similar processes may be sustained in the uDBD APPJ studied here, but further temporally resolved OES imaging studies are needed to confirm this.

Surface sampling

Finally, it is important to consider the material surface sampling/etching mechanisms that may take place. Etching with plasma jets is typically implemented with reactive gases (e.g. CF₄ or SF₆) and on materials such as silicon or polymers.⁷² However, there are several reports of APPJs with He/O2 plasma gas flowing into ambient air for polymer etching.73 In this case, the UV photons, electron impact and reactive oxygen species, such as O or OH, contribute to dissociation of molecules in the polymer, as well as formation of surface radicals that serve as starting points for the etching process.74 The high intensity O I optical emission region observed here for the LDPE sample (cf. Fig. 6) points to the significance of such mechanisms. Furthermore, the peak $T_{\rm rot}$ observed (\sim 700 K) toward the sample surface would not only enhance the etching process but may also contribute to thermal-based effects, such as melting, since softening of LDPE starts ~350 K, which probably leads to the large size of the craters observed in the LDPE sample (cf. Fig. 9b). On the other hand, the craters measured in the copper sample are much smaller (cf. Fig. 9a) and there was a clear correlation of the N2 + optical emission and the crater full width, or in the case of ring-shaped bottom craters, a correlation of the N_2^+ optical emission FWHM and the valley-to-valley distance (cf. Fig. 10). APPJs are not typically used for metal etching, but mostly metal surface treatment, such as hydrophilic/ hydrophobic modification.72 However, Kuwahata and Yamaguchi showed that an Ar DBD-based APPJ flowing into open air could be used for removing Al thin films deposited on glass slides.75 On one hand, they observe streamers from the APPJ that converge onto the sample surface and result in concave shaped craters at longer APPI/surface distances. On the other hand, at shorter APPJ/surface distances, they observe the streamers maintain the original ring-shaped structure they display flowing along the wall of the APPJ quartz tube, which results in ring-shaped craters. In our study here, a similar process may be taking place, supported by the crater shapes changing from concave to ring-shaped as the flow rate is increased, which in turn results in pushing the plasma plume OES spatial structure onto the sample surface, thus having a similar effect as bringing the APPI tube closer to the sample surface. Again, further temporally resolved OES imaging diagnostic studies are needed to confirm this and explain the

Conclusions

In this study, radially resolved OES plasma diagnostics on a He μDBD flowing onto different sample materials in the open air were successfully performed. The measured radially resolved distribution maps of representative plasma species (He I, $N_2^{}$, N_2 , He₂, O I) provided insights into energy transfer pathways and display clear differences compared to their line-of-sight counterparts, thus showing the importance of radially resolved data. The electrical studies results show that higher applied voltage or discharge gas flow rate leads to a higher conduction current, indicating more charged species are present in the active plasma region.

The main goal of this study was achieved by obtaining further insights into the underlying mechanisms changes brought upon exposing the APPJ plasma plume to different sample surfaces. The OES spatial distribution sequences between the different plasma species monitored, show that, when the plasma plume impinges on an LDPE target, similar energy transfer pathways are observed compared to its freeflowing counterpart. This means that in the upstream region of the He μ DBD, N_2^+ is produced by PI with He metastables, while downstream they are produced by CT with He₂⁺, as supported by the T_{rot} maps, followed by electron recombination to yield excited N₂. On the other hand, the OES spatial structure of the plasma plume changes significantly when it interacts with a floating copper sample, particularly at the plasma/surface interface where most species display an intensity peak. This is proposed to be due to an increased T_e and n_e close to the sample surface, which promotes electron impact excitation, that is in turn due to a faster ionization wave during the start of the positive half-cycle and the subsequent return stroke, followed by a diffuse glow-like discharge in the presence of a metal target and not observed in non-conductive targets, as reported for other APPI configurations.

Interestingly, a clear correlation between the widths of the erosion crater in the copper sample and the N_2^+ emission was observed, which indicates the nitrogen ion could play an important role in the surface erosion process and may be utilized for monitoring of such processes. Moreover, the presence of streamers originating in the plasma are proposed to be involved in the erosion process, as reported for other APPJ configurations. In addition, future studies including spatiotemporally resolved OES maps, as well as fundamental parameters maps, *e.g.* T_e and n_e , are underway to provide further insight/confirmation into some of the proposed underlying mechanisms.

It is worth noting that the observations here may be applicable to other APPJs, *e.g.* the ones typically utilized for plasmabased ambient desorption/ionization mass spectrometry, biomedical applications, surface modifications, *etc.*⁷⁶ For example, low-temperature plasma (LTP), a DBD APPJ, MS method development studies have shown that the negative ion mass spectral fingerprints of chemical warfare agents are

significantly changed when desorbed from different substrates.77 Specifically, a higher degree of fragmentation was observed when analyzing TNT (2,4,6-trinitrotoluene) on copper foil in comparison to a glass slide (seen by a significant ratio change between the $[M-H]^-$ peak at m/z 226 and a fragment ion $[M-H-NO]^-$ peak at m/z 197). This is in line with our results presented here, particularly the increased optical emission intensities near the Cu sample surface, but absent in the PTFE sample, with their proposed origin being attributed to an increase of the n_e and T_e , which would in turn result in higher degree of analyte fragmentation. However, plasma-based AMS studies on the effect of different substrates have typically focused on improvements in LODs and other analytical figures of merit, 77,78 rather than mechanistic ion formation. Therefore, there is a need to study the effect of various substrates on the underlying mechanisms responsible for MS ion formation, especially in regards to APPJs used for chemical analysis applications (e.g. µDBDs), which are the focus of current and future studies in our laboratory.

Conflicts of interest

There are no conflicts to declare.

Acknowledgements

The authors would like to acknowledge support by the National Science Foundation under CHE-1610849.

References

- 1 D. R. Baer, Surf. Interface Anal., 2012, 44, 1305-1308.
- 2 P. M. Peacock and C. N. McEwen, *Anal. Chem.*, 2004, **76**, 3417–3428.
- 3 T. Gruendling, S. Weidner, J. Falkenhagen and C. Barner-Kowollik, *Polym. Chem.*, 2010, 1, 599–617.
- 4 S. M. Weidner and S. Trimpin, *Anal. Chem.*, 2010, **82**, 4811–4829.
- 5 Z. Takáts, J. M. Wiseman, B. Gologan and R. G. Cooks, *Science*, 2004, **306**, 471.
- 6 M. C. Jecklin, G. Gamez and R. Zenobi, *Analyst*, 2009, **134**, 1629–1636.
- 7 Z. Xing, J. Wang, G. Han, B. Kuermaiti, S. Zhang and X. Zhang, *Anal. Chem.*, 2010, **82**, 5872–5877.
- 8 M. S. Heywood, N. Taylor and P. B. Farnsworth, *Anal. Chem.*, 2011, **83**, 6493–6499.
- 9 K. Sasaki, R. Engeln and E. V. Barnat, J. Phys. D: Appl. Phys., 2018, 51(4), 040202.
- 10 M. Šimek, J. Phys. D: Appl. Phys., 2014, 47(46), 463001.
- 11 L. Hood-Hong, J. Sci. Technol., 2014, 6(1), 49-66.
- 12 M. A. Song, Y. W. Lee and T. H. Chung, *Phys. Plasmas*, 2011, 18, 023504.
- 13 V. Laporta and D. Bruno, J. Chem. Phys., 2013, 138, 104319.
- 14 G. C. Y. Chan and G. M. Hieftje, *Spectrochim. Acta, Part B*, 2006, **61**, 31–41.
- 15 S. H. Nam and Y. Jo Kim, *Bull. Korean Chem. Soc.*, 2001, 22, 827–832.

JAAS Pa

- 16 J. M. Palomares, S. Hübner, E. A. D. Carbone, N. De Vries, E. M. Van Veldhuizen, A. Sola, A. Gamero and J. J. A. M. Van Der Mullen, *Spectrochim. Acta, Part B*, 2012, 73, 39–47.
- 17 S. Shi, X. Gong, Y. Mu, K. Finch and G. Gamez, *J. Anal. At. Spectrom.*, 2018, 33, 1745–1752.
- 18 S. Shi, K. Finch, Y. She and G. Gamez, *J. Anal. At. Spectrom.*, 2020, **35**, 117–125.
- 19 M. Kroschk, J. Usala, T. Addesso and G. Gamez, *J. Anal. At. Spectrom.*, 2016, **31**, 163–170.
- 20 G. Gamez, D. Frey and J. Michler, *J. Anal. At. Spectrom.*, 2012, 27, 50–55.
- 21 C. A. Schneider, W. S. Rasband and K. W. Eliceiri, *Nat. Methods*, 2012, **9**, 671–675.
- 22 H. D. Yang, K. X. Chen, Q. S. He and G. F. Jin, *Spectrosc. Spectral Anal.*, 2009, **29**, 3169–3172.
- 23 C. Pernechele, L. Poletto, P. Nicolosi and G. Naletto, *Opt. Eng.*, 1996, 35, 1503–1510.
- 24 G. Pretzler and Z. Naturfors, *Z. Naturforsch., A: Phys. Sci.*, 1991, **46**, 639–641.
- 25 Y. Hong, N. Lu, J. Pan, J. Li and Y. Wu, *Thin Solid Films*, 2013, 531, 408–414.
- 26 F. J. Gordillo-Vázquez, M. Camero and C. Gómez-Aleixandre, Plasma Sources Sci. Technol., 2005, 15, 42–51.
- 27 N. U. Rehman, A. Masood, Z. Anjum, I. Ahmad, M. A. Khan and M. Zakaullah, *Radiat. Eff. Defects Solids*, 2015, **170**, 668–678.
- 28 A. N. Goyette, W. B. Jameson, L. W. Anderson and J. E. Lawler, J. Phys. D: Appl. Phys., 1996, 29, 1197–1201.
- 29 A. N. Goyette, J. R. Peck, Y. Matsuda, L. W. Anderson and J. E. Lawler, *J. Phys. D: Appl. Phys.*, 1998, **31**, 1556–1564.
- 30 Inductively Coupled Plasma Emission Spectroscopy, Part 2: Applications and Fundamentals, ed. P. W. J. M. Boumans, Wiley, New York, 1987.
- 31 J. Luque and D. R. Crosley, Computer program by SRI International, SRI report No. MP 99-009, 1999.
- 32 G. C. Chan, J. T. Shelley, J. S. Wiley, C. Engelhard, A. U. Jackson, R. G. Cooks and G. M. Hieftje, *Anal. Chem.*, 2011, 83, 3675–3686.
- 33 A. Kramida, Y. Ralchenko, J. Reader and NIST ASD Team, NIST Atomic Spectra Database (version 5.8), National Institute of Standards and Technology, Gaithersburg, MD, 2020, DOI: 10.18434/T4W30F.
- 34 E. A. D. Carbone, C.-G. Schregel and U. Czarnetzki, *Plasma Sources Sci. Technol.*, 2016, **25**(5), 054004.
- 35 R. W. B. Pearse and A. G. Gaydon, *The Identification of Molecular Spectra*, John Wiley & Sons, New York, 4th edn, 1976, pp. 16-19.
- 36 U. N. Pal, A. K. Sharma, J. S. Soni, S. Kr, H. Khatun, M. Kumar, B. L. Meena, M. S. Tyagi, B. J. Lee, M. Iberler, J. Jacoby and K. Frank, J. Phys. D: Appl. Phys., 2009, 42(4), 045213.
- 37 Z. Hao, S. Ji, H. Liu and Y. Song, *IEEE Trans. Plasma Sci.*, 2014, **42**, 824–832.
- 38 K. Gazeli, P. Svarnas, P. Vafeas, P. K. Papadopoulos, A. Gkelios and F. Clément, *J. Appl. Phys.*, 2013, 114, 103304.

- 39 B. Brutschy and H. Haberland, *Phys. Rev. A: At., Mol., Opt. Phys.*, 1979, 19, 2232–2248.
- 40 R. Deloche, P. Monchicourt, M. Cheret and F. Lambert, *Phys. Rev. A: At., Mol., Opt. Phys.*, 1976, **13**, 1140.
- 41 J. Stevefelt, J. Pouvesle and A. Bouchoule, *J. Chem. Phys.*, 1982, **76**, 4006–4015.
- 42 L. Alves, G. Gousset and C. Ferreira, J. Phys. D: Appl. Phys., 1992, 25, 1713.
- 43 Y. B. Golubovskii, V. Maiorov, J. Behnke and J. Behnke, *J. Phys. D: Appl. Phys.*, 2002, **36**, 39.
- 44 S. A. Norberg, E. Johnsen and M. J. Kushner, *J. Appl. Phys.*, 2015, **118**, 013301.
- 45 J. S. Furter and P. C. Hauser, *Anal. Methods*, 2018, **10**, 2701–2711
- 46 I. Dzidic, D. I. Carroll, R. N. Stillwell and E. C. Horning, *Anal. Chem.*, 1976, **48**, 1763–1768.
- 47 E. Horning, D. Carroll, I. Dzidic, K. Haegele, M. Horning and R. Stillwell, *J. Chromatogr. Sci.*, 1974, **12**, 725–729.
- 48 H. Kambara, Y. Mitsui and I. Kanomata, *Anal. Chem.*, 1979, **51**, 1447–1452.
- 49 A. Qayyum, S. Zeb, M. A. Naveed, S. A. Ghauri, A. Waheed and M. Zakaullah, *Plasma Devices Oper.*, 2006, **14**, 61–70.
- 50 S. C. Ostrander and J. C. Weisshaar, Chem. Phys. Lett., 1986, 129, 220–224.
- 51 T. Martens, D. Mihailova, J. van Dijk and A. Bogaerts, *Anal. Chem.*, 2009, **81**, 9096–9108.
- 52 S. B. Olenici-Craciunescu, A. Michels, C. Meyer, R. Heming, S. Tombrink, W. Vautz and J. Franzke, *Spectrochim. Acta, Part B*, 2009, 64, 1253–1258.
- 53 S. B. Olenici-Craciunescu, S. Müller, A. Michels, V. Horvatic, C. Vadla and J. Franzke, *Spectrochim. Acta, Part B*, 2011, 66, 268–273.
- 54 M. Endoh, M. Tsuji and Y. Nishimura, *J. Chem. Phys.*, 1983, **79**, 5368–5375.
- 55 W. Richardson and D. Setser, *J. Chem. Phys.*, 1973, **58**, 1809–1825.
- 56 P. M. Mul and J. W. McGowan, J. Phys. B: At. Mol. Phys., 1979, 12, 1591–1601.
- 57 R. Zaplotnik, M. Bišćan, D. Popović, M. Mozetič and S. Milošević, *Plasma Sources Sci. Technol.*, 2016, **25**, 035023.
- 58 B. L. M. Klarenaar, O. Guaitella, R. Engeln and A. Sobota, *Plasma Sources Sci. Technol.*, 2018, 27, 085004.
- 59 W. E. Curtis, Proc. R. Soc. London, Ser. A, 1913, 89, 146-149.
- 60 P. C. Hill, Phys. Rev. A: At., Mol., Opt. Phys., 1989, 40, 5006–5016.
- 61 W. G. Rellergert, S. B. Cahn, A. Garvan, J. C. Hanson, W. H. Lippincott, J. A. Nikkel and D. N. McKinsey, *Phys. Rev. Lett.*, 2008, **100**, 025301.
- 62 R. J. Van Sonsbeek, R. Cooper and R. N. Bhave, *J. Chem. Phys.*, 1992, **97**, 1800–1806.
- 63 J. B. Gerardo and M. A. Gusinow, *Phys. Rev. A: At., Mol., Opt. Phys.*, 1971, 3, 255–267.
- 64 P. L. Patterson, J. Chem. Phys., 1968, 48, 3625-3631.
- 65 T. Martens, A. Bogaerts, W. J. M. Brok and J. J. A. M. van der Mullen, *J. Anal. At. Spectrom.*, 2007, 22(9), 1033–1042.
- 66 T. Martens, A. Bogaerts, W. Brok and J. van Dijk, *Anal. Bioanal. Chem.*, 2007, **388**, 1583–1594.

- 67 P. C. Cosby, J. Chem. Phys., 1993, 98, 9560-9569.
- 68 G. B. Rusu, A. V. Nastuta, A. S. Chiper and G. Popa, On the discharge parameters of a glow mode DBD, On the discharge parameters of a glow mode DBD, 23rd International Symposium on Discharges and Electrical Insulation in Vacuum, DOI: 10.1109/ 2008, 619-622, DEIV.2008.4676875.
- 69 D. Riès, G. Dilecce, E. Robert, P. F. Ambrico, S. Dozias and J. M. Pouvesle, J. Phys. D: Appl. Phys., 2014, 47, 275401.
- 70 J. Winter, J. S. Sousa, N. Sadeghi, A. Schmidt-Bleker, S. Reuter and V. Puech, Plasma Sources Sci. Technol., 2015, 24, 025015.
- 71 A. Schmidt-Bleker, S. A. Norberg, J. Winter, E. Johnsen, S. Reuter, K. D. Weltmann and M. J. Kushner, Plasma Sources Sci. Technol., 2015, 24(3), 035022.

- 72 F. Fanelli and F. Fracassi, Surf. Coat. Technol., 2017, 322, 174-201.
- 73 K. Nakazawa, S. Yamamoto, E. Nakagawa, A. Ogino, M. Shimomura and F. Iwata, AIP Adv., 2020, 10, 095103.
- 74 K. Fricke, H. Steffen, T. von Woedtke, K. Schröder and K.-D. Weltmann, Plasma Processes Polym., 2011, 8, 51-58.
- 75 H. Kuwahata and T. Yamaguchi, e-J. Surf. Sci. Nanotechnol., 2016, 14, 231-236.
- 76 M. Hofmans, P. Viegas, O. v. Rooij, B. Klarenaar, O. Guaitella, A. Bourdon and A. Sobota, Plasma Sources Sci. Technol., 2020, 29, 034003.
- 77 Y. Zhang, X. Ma, S. Zhang, C. Yang, Z. Ouyang and X. Zhang, Analyst, 2009, 134, 176-181.
- 78 J. F. Garcia-Reyes, J. D. Harper, G. A. Salazar, N. A. Charipar, Z. Ouyang and R. G. Cooks, Anal. Chem., 2011, 83, 1084-1092.